nuclear fusion
IAEA

PAPER

# The phase-space dependence of fast-ion interaction with tearing modes

To cite this article: W.W. Heidbrink *et al* 2018 *Nucl. Fusion* **58** 082027

View the article online for updates and enhancements.

This content was downloaded from IP address 192.188.106.50 on 10/07/2018 at 19:15

IOP Publishing | International Atomic Energy Agency Nuclear Fusion

Nucl. Fusion **58** (2018) 082027 (16pp) https://doi.org/10.1088/1741-4326/aab7b6

# The phase-space dependence of fast-ion interaction with tearing modes[a]

**W.W. Heidbrink[1], L. Bardoczi[2], C.S. Collins[3], G.J. Kramer[4], R.J. La Haye[3], D.J. Lin[1], C.M. Muscatello[3], M. Podestà[4], L. Stagner[1], M.A. Van Zeeland[3] and Y.B. Zhu[1]**

[1] University of California, Irvine, Irvine, CA, United States of America
[2] Oak Ridge Associated Universities, Oak Ridge, TN, United States of America
[3] General Atomics, San Diego, CA, United States of America
[4] Princeton Plasma Physics Laboratory, Princeton, NJ, United States of America

E-mail: wwheidbr@uci.edu

Received 26 December 2017, revised 17 February 2018
Accepted for publication 19 March 2018
Published 3 July 2018

**Abstract**

Modulation of various neutral beam sources probes the interaction of fast ions with tearing modes (TM) in the DIII-D tokamak. As measured by electron cyclotron emission, the $(m, n) = (2, 1)$ tearing modes have an island width of $\sim$8 cm and change phase 180° at the $q = 2$ surface. (Here, $m$ is the poloidal mode number and $n$ is the toroidal mode number.) Deuterium neutral beam injection by six sources with differing injection geometries produces the fast ions. To study the interaction in different parts of phase space, on successive discharges, one of the six sources is modulated at 20 Hz to populate different fast-ion orbits. The modulation only changes the island width by a few millimeters, implying that any fast-ion effect on mode stability is below detection limits. When compared to the expected signals in the absence of TM-induced transport, both the average and modulated neutron signals deviate, implying that fast-ion transport occurs in much of phase space. Fast-ion $D_\alpha$ (FIDA) measurements detect reductions in signal at wavelengths that are sensitive to counter-passing ions. Neutral particle analyzer data imply poor confinement of trapped fast ions. Calculations of the expected fast-ion transport that use measured TM properties successfully reproduce the data.

Keywords: tearing modes, fast ions, FIDA

(Some figures may appear in colour only in the online journal)

## 1. Introduction

Tearing modes (TMs) are often unstable in tokamak plasmas. Usually, they are detrimental, degrading confinement or triggering disruptions. But TMs can also be beneficial: In the 'hybrid' regime [1, 2], TMs help sustain a favorable profile of the safety factor $q$.

Degradation of fast-ion confinement by large tearing modes was established decades ago [3]. Subsequent quantitative work compared neutron [4] and loss detector [5–7] signals with theoretical predictions. In these studies, an orbit code followed fast ions in model TMs with amplitudes that were matched to experimental measurements; consistency between theory and experiment was reported. In theory, the orbits of circulating ions can become stochastic when the combination of TM island width and fast-ion curvature drift exceed a certain threshold [8, 9]. This threshold was exceeded in some experiments that exhibited reduced neutral-beam current drive and neutron rates [10]. For trapped ions, Marchenko and Lutsenko [11] predicted that resonance of the precession frequency with the mode causes losses of trapped fast ions.

TMs may affect fast ions but the opposite is also true: Fast ions can impact TM stability. One theoretical paper claims

[a] IAEA Technical Meeting paper for submission to Nuclear Fusion

 © 2018 IAEA, Vienna Printed in the UK

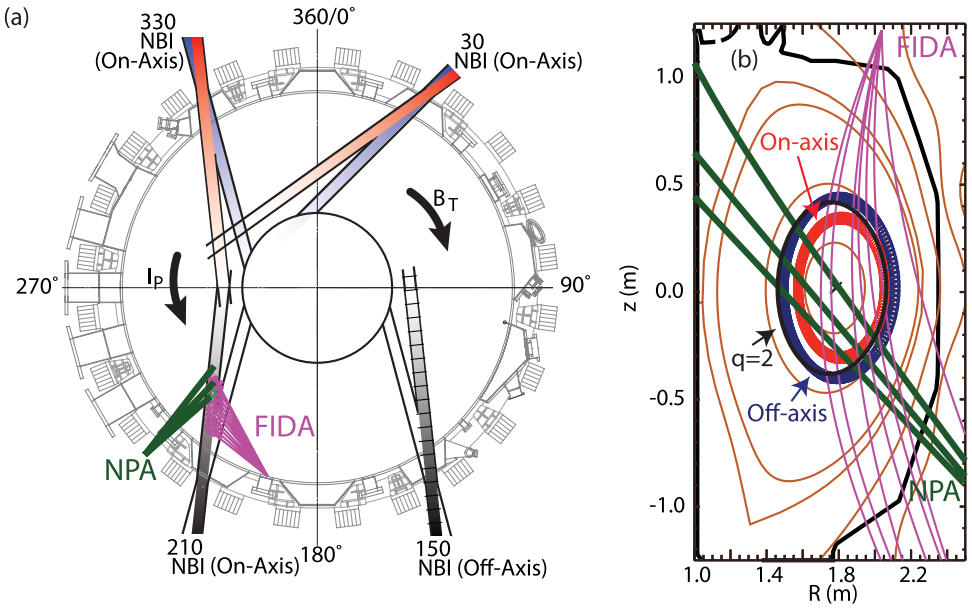


**Figure 1.** (*a*) Plan view of the DIII-D tokamak, showing the orientation of the eight neutral beam sources, the direction of the toroidal field $B_T$ and plasma current $I_p$, and projections of the FIDA and SSNPA sightlines. (*b*) Elevation of DIII-D, showing flux surfaces for a typical equilibrium and the location of the $q = 2$ surface. Orbits from the On/Co/Tang and Off/Co/Tang beams that ionize near the $q = 2$ surface are also shown.

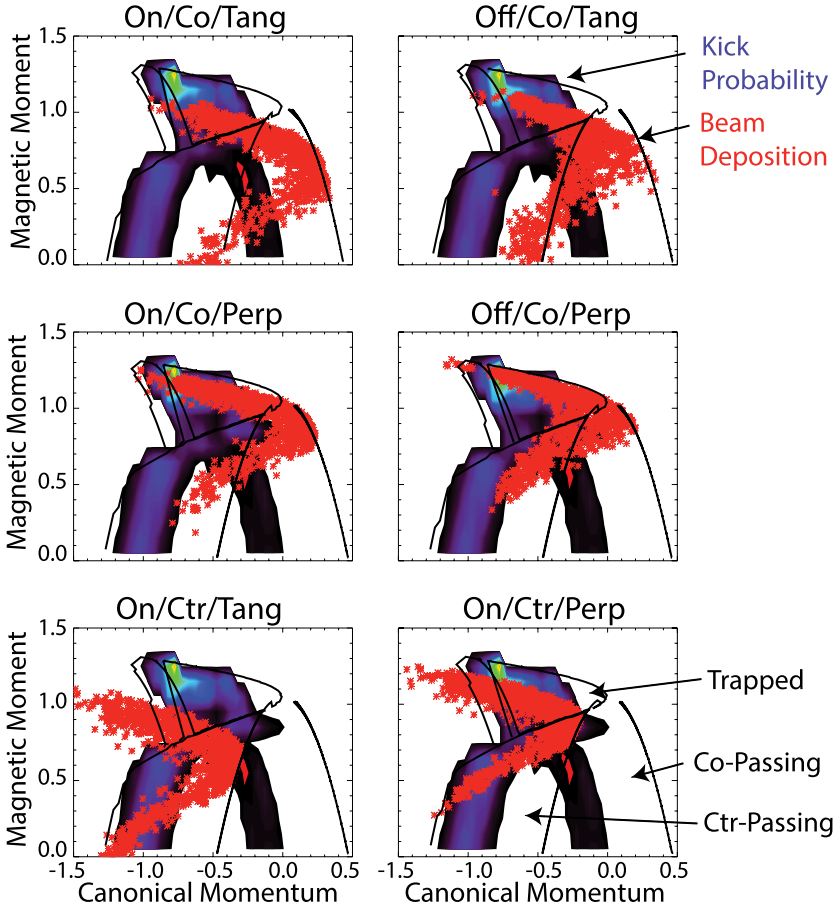


**Figure 2.** Beam deposition (x) in constants-of-motion space for the six different beam orientations. The abscissa is the toroidal canonical momentum $P_\phi$ normalized to the poloidal flux difference between the magnetic axis and the last closed flux surface. The ordinate is the normalized magnetic moment $\mu B_0/E$, where $B_0$ is the central magnetic field and $E$ is the ion energy. Topological boundaries are indicated by solid lines. The contour plot shows the rms magnitude of the energy kick probabilities used in the TRANSP kick modeling.

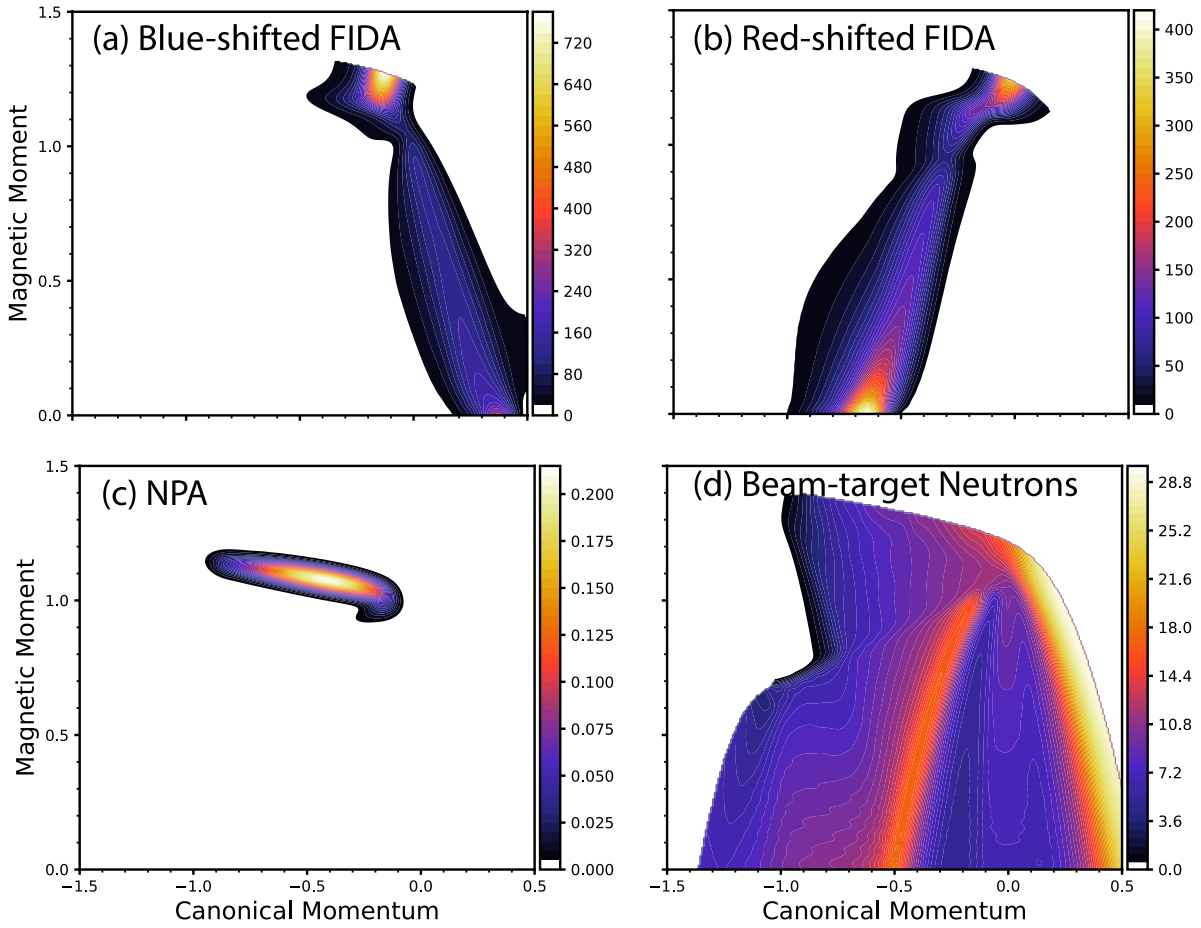


**Figure 3.** Weight functions for (*a*) blue-shifted and (*b*) red-shifted signals from the FIDA channel at $R = 193$ cm after integration over 651.1–652.7 nm and 659.5–661.1 nm, respectively. (*c*) Weight function for the $R = 165$ cm NPA channel. (*d*) Beam-target contribution to the volume-averaged neutron weight function. The neutron signal is also sensitive to beam–beam reactions but this sensitivity is not shown. As in figure 2, the abscissa is the normalized toroidal canonical angular momentum and the ordinate is the normalized magnetic moment.

circulating fast ions drive helical currents that are destabilizing if the fast ions are inside the rational surface but stabilizing if they are outside [12]. Another paper argues that 'co-circulating' fast ions that travel in the direction of the plasma current are stabilizing [13], while counter-passing and trapped ions are destabilizing [14]. A recent paper states that energetic particles alter the bootstrap current that drives TMs through an uncompensated cross-field current associated with orbit effects; the predicted effect is most important in plasmas with reversed shear [15]. For tokamaks, no definitive experimental demonstration of the effect of fast ions on stability exists but numerous observations are suggestive. In both ASDEX Upgrade [16] and TFTR [17], TMs were observed to chirp several kHz in frequency. In EAST, small oscillations in mode frequency are attributed to interaction with fast ions [18]. In the reversed-field pinch, neutral-beam injection reduced the amplitude of $(m, n) = (1, 5)$ tearing modes 60% [19].

Recently, a new technique to probe fast-ion transport in different parts of phase space was developed [20] and used to measure fast-ion transport by Alfvén eigenmodes [21–23]. Phase-space sensitivity is obtained in two ways: by modulating beams that populate different parts of phase space and by utilizing fast-ion diagnostics with different phase-space sensitivities. In this paper, the beam modulation technique is applied to DIII-D discharges with large $(m, n) = (2, 1)$ TMs. (Here, $m$ is the poloidal mode number and $n$ is the toroidal mode number.) The experimental conditions and analysis methods are described in section 2. Section 3 considers the effect of the fast ions on TM stability. Measurements and modeling of fast-ion transport by TMs are reported in section 4. Discussion and conclusions are in section 5. An appendix documents the calculation of phase-space sensitivities.

## 2. Experimental conditions

The experiment is conducted in neutral-beam heated deuterium plasmas in the DIII-D tokamak. All of the data in this paper are from a single day of operation. For the experiment, the eight deuterium neutral beam sources inject in six different directions (figure 1(*a*)). Six sources inject in the direction of the plasma current and two inject in the counter-current direction; six inject in the midplane and two inject below the midplane; four inject at a near-tangential angle and four inject at a near-perpendicular angle. For the off-axis sources, the field helicity is in the direction that creates trapped orbits as well

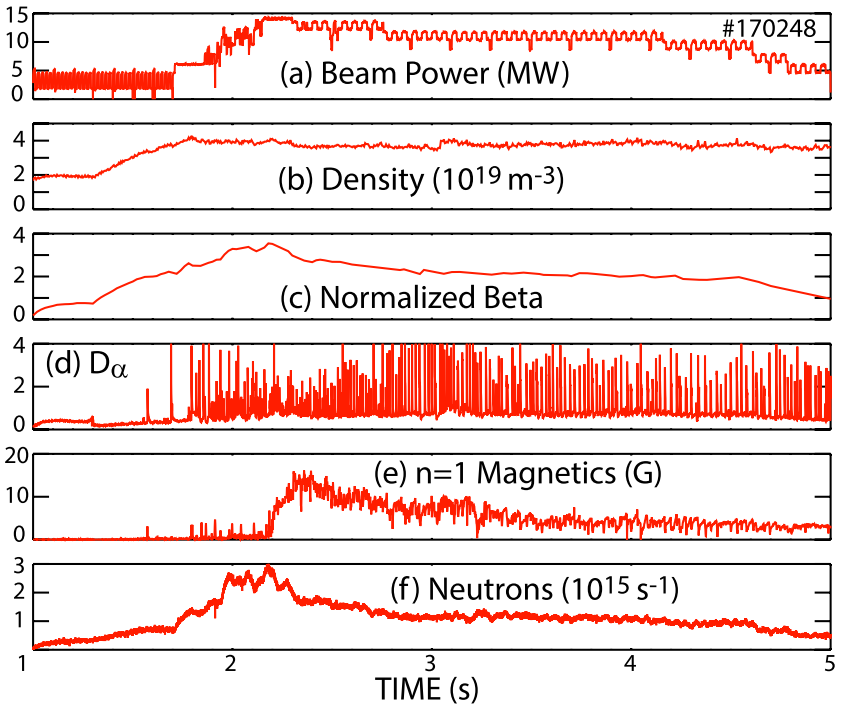


**Figure 4.** Time evolution of (*a*) beam power, (*b*) line-average electron density, (*c*) normalized beta $\beta_N = \beta_T/(I/aB_T)$, (*d*) cold $D_\alpha$ light from the divertor, (*e*) midplane magnetics $n = 1$ magnetics signal, and (*f*) neutron rate in a typical discharge. $B_T = 2.0$ T; $I_p = 0.8$ MA.

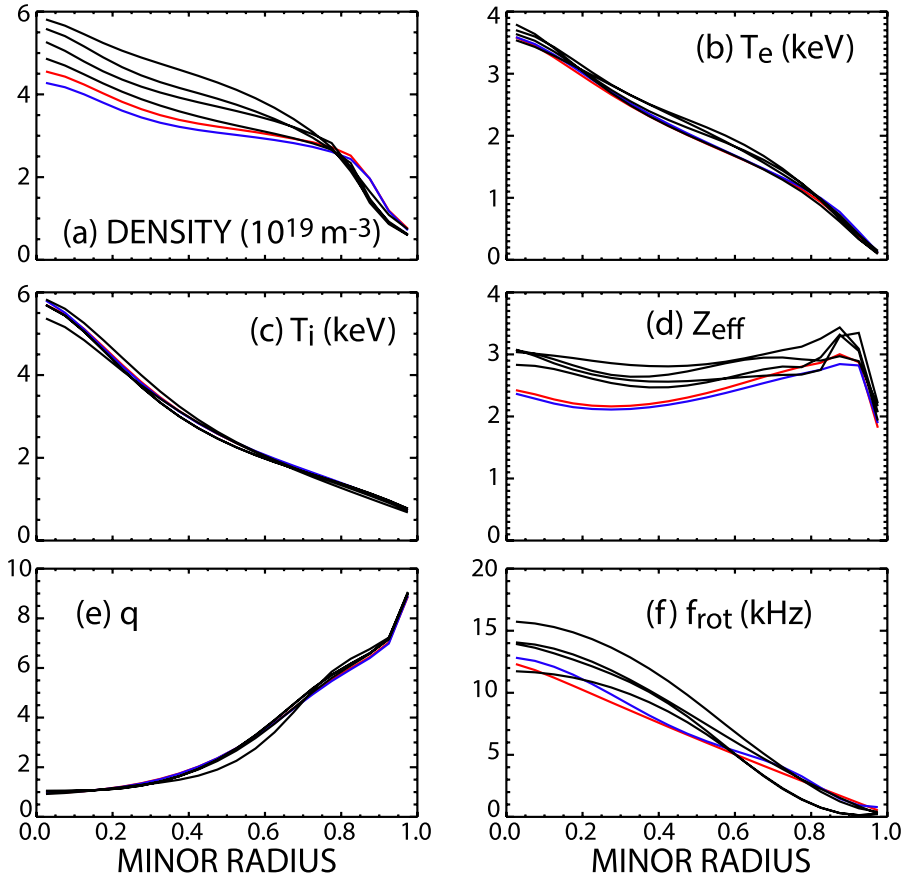


**Figure 5.** Plasma profiles (averaged between 2.4–2.8 s) on six discharges with modulated beams of different orientations. (*a*) Electron density, (*b*) electron temperature, (*c*) ion temperature, (*d*) $Z_{eff}$, (*e*) $q$ profile, and (*f*) toroidal rotation. The minor radius coordinate $\rho$ is the normalized square root of the toroidal flux.

as passing orbits [24]. The plasma shape is an elongated lower single null divertor configuration (figure 1(*b*)). The on-axis sources deposit particles on both sides of the $q = 2$ surface but only the most deeply deposited orbits from the off-axis sources intersect the $q = 2$ surface.

The phase-space dependence of the interaction between TMs and fast ions is investigated by modulating different sources and by interrogating the plasma with diagnostics that are sensitive in different parts of phase space. As shown in figure 2, different angles of injection deposit fast ions in different parts of phase space. (The 'kick' probabilities in figure 2 are discussed later.) Fast-ion diagnostics include the volume-averaged neutron rate, fast-ion D-alpha (FIDA) from oblique views [25], and three solid-state neutral particle analyzers (NPA) operated in current mode [26] that view primarily trapped particles. The FIDA and NPA sightlines are shown in figure 1. The counter-tangential source is the active beam for these diagnostics. In this paper, the FIDA and NPA channels are identified by the major radius of intersection of the sightline with the active beam at the midplane.

The phase-space sensitivities or 'weight functions' [27] of representative channels are shown in figure 3. Blue-shifted FIDA measurements are most sensitive to co-passing ions, red-shifted FIDA measurements are most sensitive to counter-passing ions, the NPA measurements are most sensitive to trapped ions, and the neutron diagnostic is sensitive throughout the high energy portion of phase space. (Details of the weight function calculations appear in the appendix.)

To trigger a $(2, 1)$ TM, a burst of beam power is injected from 1.96–2.16 s, after which the power is reduced to 10–13 MW to avoid a disruption (figure 4). Fairly steady conditions persist for several seconds after the power burst. During this phase, one source is modulated with 50 ms period. On repeat shots, a different source is modulated. Edge localized modes (ELMs) persist throughout (figure 4(*d*)).

Analysis is based on similar shots that each have a different modulated beam. Plasma profiles for six of these discharges are compared in figure 5. The electron density, which is measured by interferometers [28] and a profile reflectometer [29], differs by $\sim\pm 15\%$ over these discharges (figure 5(*a*)). The electron temperature $T_e$, which is measured by Thomson scattering [30] and by an electron cyclotron emission (ECE) radiometer [31], is well matched on the six shots (figure 5(*b*)), as is the ion temperature measured by carbon charge-exchange recombination spectroscopy (CER) [32] (figure 5(*c*)). $Z_{\rm eff}$, as determined from carbon CER measurements in the graphite-wall DIII-D, is relatively large but similar in the six shots (figure 5(*d*)). The $q$ profile from EFIT [33] reconstructions that utilize motional Stark effect [34] data is similar in all discharges (figure 5(*e*)). The toroidal rotation profile from CER varies $\sim\pm 20\%$ (figure 5(*f*)).

The tearing modes are diagnosed by magnetics and ECE. The toroidal and poloidal mode numbers, as measured by toroidal and poloidal arrays of magnetic probes [35], are $n = 1$ and $m = 2$, respectively. As expected for a resistive mode, the phase of the ECE signals from a radial radiometer array changes by $\sim 180°$ at the rational surface (figure 6(*b*)). Also as

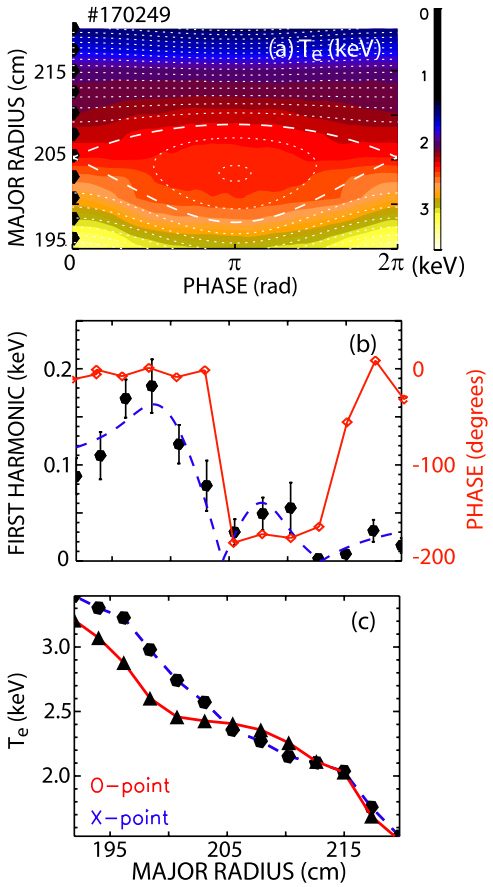


**Figure 6.** ECE measurement of the island width at 2.79 s. (*a*) Contour plot of the electron temperature after mapping from time to phase. The dashed line is the inferred separatrix. (*b*) Amplitude (solid circle) and phase (square) of $\tilde{T}_e$ at the fundamental TM frequency (12.7 kHz) versus major radius. The dashed line is the fit to the island model. (*c*) Profiles of $T_e$ at the O-point and X-point.

expected, the largest mode amplitude of the ECE radial eigenfunction is centered at the $q = 2$ surface inferred from the equilibrium reconstruction (figure 6(*b*)). In addition, the ECE imaging diagnostic [36] measures a poloidal structure that is consistent with a poloidal mode number of $m = 2$. Because the plasma rotates, temporal variations in the ECE data from the radial radiometer array can be interpreted in terms of the phase of the island (figure 6(*a*)). (On a few discharges, the plasma transiently locked for a portion of the time of interest; these time periods are excluded from the analysis.) The measured $T_e$ profiles are interpreted in terms of a model that takes into account finite cross-field transport [37]. As quantified by the reduced $\chi^2$, the model provides a good fit to the data for most time slices.

Magnetics data provide an independent measurement of the mode width. In a multipole approximation and taking into account that the wall boundary condition for a rotating mode effectively doubles the measured poloidal field [38], the island width $W(t)$ is

$$W(t) = \sqrt{\frac{8 f_\theta L_q(r_s,t) R_0(t) |\tilde{B}_\theta(r_s,t)|}{n B_\phi(r_s,t)}} \left( \frac{R_0(t) - R_{\rm probe}}{r_s(t)} \right)^{m+1}. \quad (1)$$

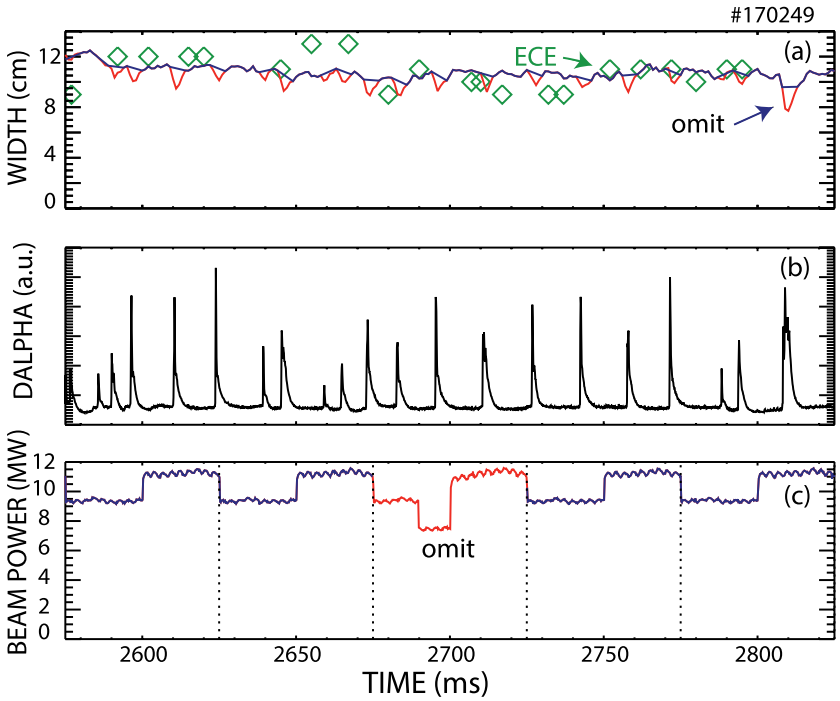


**Figure 7.** Time evolution of (*a*) island widths from ECE (as in figure 6) and from magnetics (equation (1)), (*b*) cold $D_\alpha$ light from the divertor, and (*c*) beam power in a typical discharge. Width measurements at the time of ELM bursts are excluded from the conditional averaging, as are cycles with power variations in more than one beam.

Here, the magnetic shear length-scale $L_q$, magnetic axis $R_0$, radius of the $q = 2$ surface $r_s$, and toroidal magnetic field $B_\phi$ are inferred from the equilibrium. $\tilde{B}_\theta$ is the fluctuating poloidal field measured by a magnetic loop near the midplane at a major radius $R_{\rm probe}$. On each discharge, the geometric fitting parameter $f_\theta$ (of order unity) is selected to be consistent with the ECE measurements of the island width; the chosen values are similar for all of the discharges in this study. Typically, the detected magnetic signal $\tilde{B}_\theta$ decreases during the discharge, as in figure 4(*d*), but the inferred island width remains approximately constant, as in figure 7(*a*). The decreasing probe signal is caused by gradual evolution of the current profile. For example, for the case of figure 4, the $q = 2$ surface migrates from a normalized minor radius of $\rho = 0.46$ to $\rho = 0.39$ between 2.4 and 4.1 s.

The two measurements of island width are roughly consistent (figure 7(*a*)) but the island width from magnetics has better temporal resolution and less variability than the island width from ECE so the conditionally-averaged island width shown in section 3 utilizes the magnetics data. ELMs reduce the island width inferred from equation (1). To avoid contamination associated with ELMs, when conditionally averaging, $W(t)$ is interpolated across ELM bursts (figure 7(*a*)).

During some modulation cycles, another beam also changes. Sometimes this is due to a neutral-beam fault, sometimes this is a pre-programmed variation to accommodate active-beam diagnostics. In order to study the effect of a single neutral-beam source, cycles with multiple beam variations are excluded from the averaging (figure 7(*c*)). Throughout the paper, the signals are linearly detrended prior to conditional averaging, then the difference between the signal $s$ and the average value during that cycle $\bar{s}$ are organized into an ensemble of measurements at different phases of the cycle. The plotted points are the average value of $s - \bar{s}$; the error bars represent the deviation of the mean during the cycle for the ensemble of valid modulation periods $\sigma/\sqrt{N_{\rm per}}$, where $\sigma$ is the standard deviation of the points at each phase of the cycle and $N_{\rm per}$ is the number of cycles.

All discharges included in this study have large rotating $(2, 1)$ tearing modes with similar properties. In addition, most discharges have other low-frequency activity during many cycles that are included in the averaging. In many cases, there is another resistive $n = 1$ instability at larger radius with a frequency less than half the frequency of the $(2, 1)$ mode. Some cases have a $(3, 2)$ or $(5, 2)$ mode that may (or may not) rotate with the primary $(2, 1)$ mode.

Another complication is the presence of Alfvén eigenmodes (AE) in all of the discharges. Figures 8(*b*) and 9(*b*) show typical spectra. The modes between ~70–300 kHz are Alfvén eigenmodes. AEs have been extensively studied in DIII-D [22, 23] and are known to modify the fast-ion distribution function and cause spatial transport, an unwanted effect in this experiment.

Conveniently, despite otherwise similar conditions, one discharge did *not* have a (2,1) TM. Figure 8(*a*) compares the neutron rate in this discharge with the 'classical' neutron rate predicted by the TRANSP NUBEAM code [39]; figure 9(*a*) shows the same comparison for a representative discharge that has a (2,1) TM. This 'classical' prediction realistically treats atomic physics, Coulomb collisions, and finite orbit effects but neglects all transport associated with instabilities. Early in both discharges, the measurement is in excellent agreement

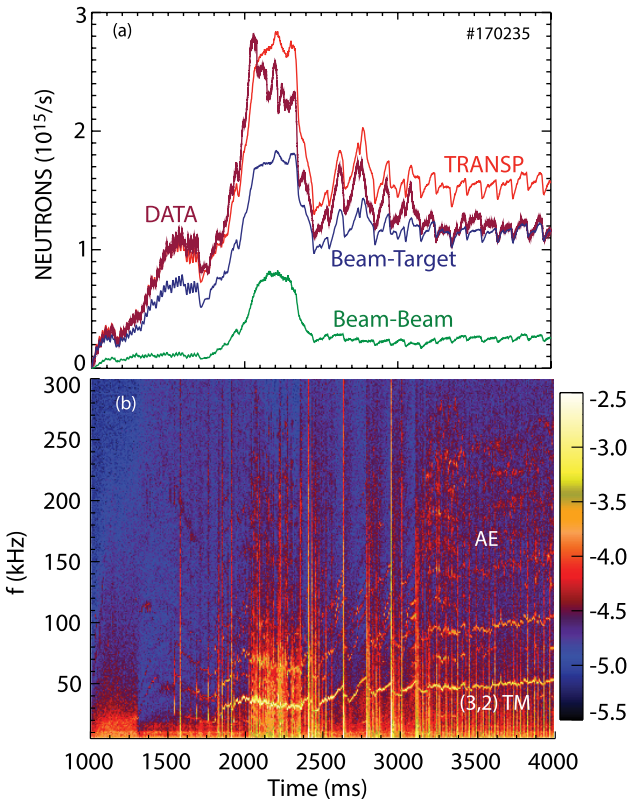


**Figure 8.** (*a*) Measured and calculated neutron rates in the reference discharge with (3, 2) TM activity. The TRANSP prediction is for the classical neutron rate and the relative contributions of beam-target and beam–beam reactions. (*b*) Cross-power of radial and vertical interferometer chords on a logarithmic scale. The strong mode at ∼37 kHz (in the latter half of the discharge) is the TM. The modes in the 100–300 kHz range are in the AE band. (The nominal Doppler-shifted TAE frequency of an $n = 3$ mode in this discharge is ∼180 kHz.)

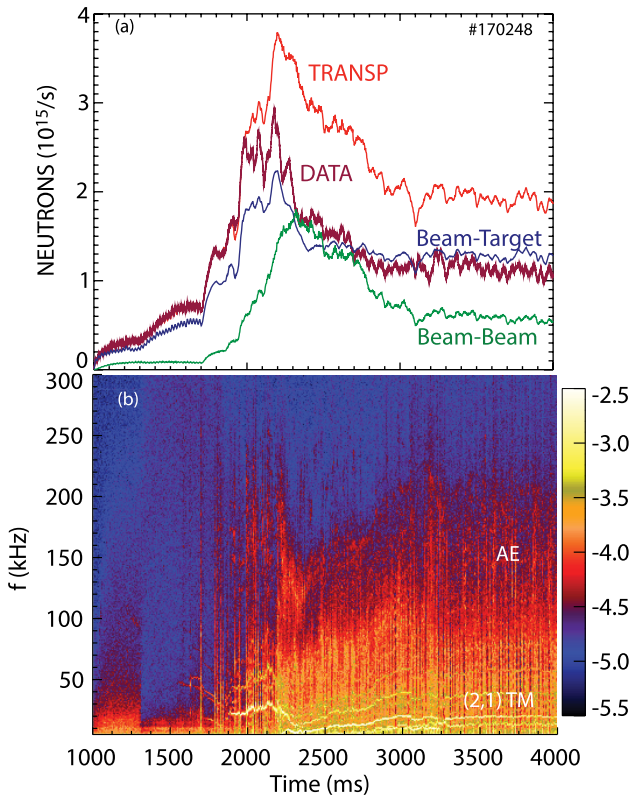


**Figure 9.** (*a*) Measured and calculated neutron rates in a representative discharge with (2,1) TM activity. The TRANSP prediction is for the classical neutron rate and the relative contributions of beam-target and beam–beam reactions. (*b*) Cross-power of radial and vertical interferometer chords; the contour scale is the same as in figure 8. The mode at ∼19 kHz in the latter half of the discharge is the dominant (2,1) TM. In this discharge, BAE activity may extend down to ∼70 kHz.

with the classical prediction; prior to the burst in beam power at 1.9 s, the plasma is essentially free of MHD activity. This agreement confirms the consistency of the TRANSP modeling with the absolute neutron calibration for data acquired during this experiment. In the reference discharge, a core (3, 2) TM becomes unstable at the power burst and persists throughout the remainder of the discharge; also, the AE activity becomes stronger after ∼3.1 s. On the shot with (2,1) activity (figure 9), following the power burst, AE and TM activity persist for the entire discharge and, after 2.4 s, the measured neutron rate is only ∼0.6 of the predicted rate. The suppressed neutron rate relative to the classical prediction indicates that the instabilities degrade the fast-ion confinement.

TRANSP classifies the neutron source as 'beam–beam' when the reactions occur between fast ions, 'beam-target' when the reactions occur between a fast ion and a thermal ion, and 'thermonuclear' when the reactions occur within the thermal ion population. Figures 8(*a*) and 9(*a*) show that the calculated beam–beam contribution is relatively large, a consequence of the strong beam heating at modest electron density employed in these discharges.

Previous work [40] used the integrated cross-power of two interferometer chords in the AE frequency band to quantify the strength of AE activity; relative to classical predictions, a strong correlation of 'AE power' with reductions in fast-ion signals was found. (In that study with dominant AE-induced transport, the reductions correlated only weakly with TM amplitudes.) Figure 10 uses this 'AE power' measurement to quantify the effect of the AE activity on the neutron measurement. As previously mentioned, all (2,1) discharges in this study have AE activity, as does the reference discharge with (3, 2) activity. Figure 10 shows that the degradation in neutron rate is largely independent of the strength of the AE activity. As expected, the neutron shortfall is larger in the discharges with large (2, 1) modes than in the reference (3, 2) discharge. From this weak scaling, we estimate that the AE activity causes a ∼10% reduction in the neutron rate, with the majority of the reduction being caused by the TMs. A 10% reduction in the neutron rate is comparable to the uncertainty in the classical TRANSP prediction associated with measurement uncertainties in $n_e$, $T_e$, and $Z_{\rm eff}$.

## 3. Effect of fast ions on TM stability

Conditionally-averaged measurements of the island width for six different beam orientations are shown in figure 11. If a particular source affects stability, one expects a waveform with a fundamental period of 50 ms, as discussed below. Figure 11

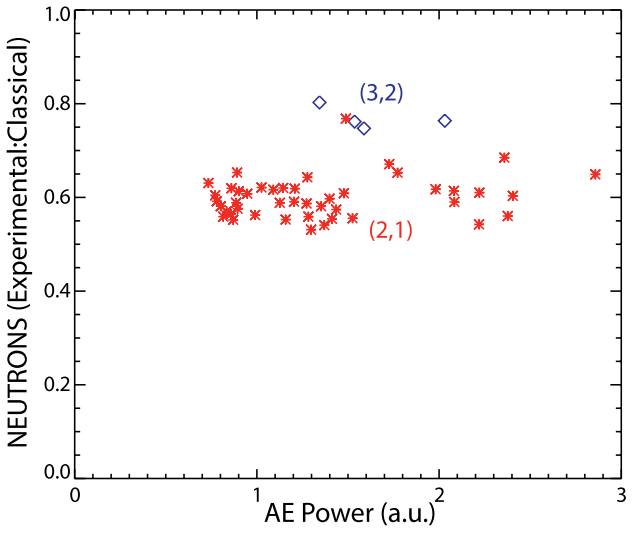


**Figure 10.** Ratio of measured neutron rate to classical prediction versus AE power at several different times for the discharges in this study (x) and for the reference discharge with only a (3,2) TM (⋄).

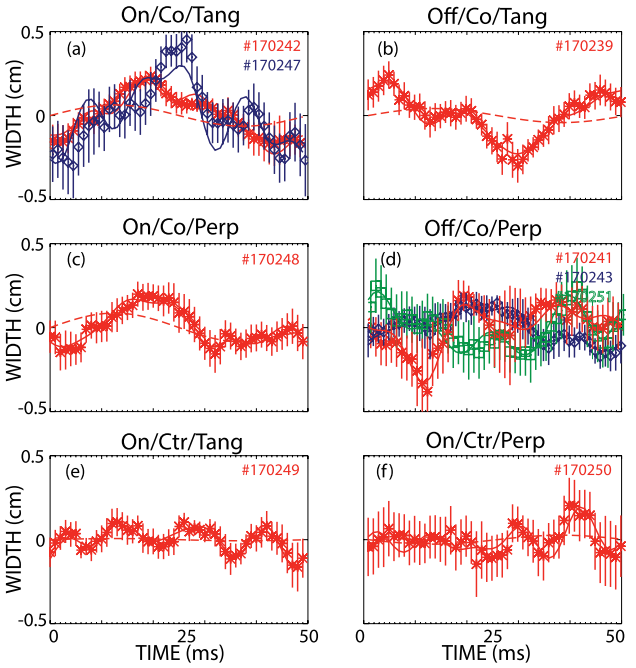


**Figure 11.** Conditionally-averaged widths for the six different beam orientations. The modulated beam is on in the first half of the cycle and off in the second half so, relative to the average power, the modulated power is positive from 0–25 ms and negative from 25–50 ms. (*a*) On-axis, co-current, near-tangential injection. The island width during the averaging period (mean and standard deviation) is $W = 6.4 \pm 0.5$ and $9.3 \pm 1.6$ cm for the two plotted discharges. (*b*) Off-axis, co-current, near-tangential injection; $W = 7.2 \pm 2.2$ cm. (*c*) On-axis, co-current, near-perpendicular injection; $W = 7.3 \pm 1.3$ cm. (*d*) Off-axis, co-current, near-perpendicular injection; $W = 10.3 \pm 1.2$, $7.5 \pm 0.8$ cm, and $6.3 \pm 1.3$ cm for the three plotted discharges. (*e*) On-axis, counter-current, near-tangential injection; $W = 8.8 \pm 0.7$ cm. (*f*) On-axis, counter-current, near-perpendicular injection; $W = 8.6 \pm 1.6$ cm. The solid lines are nonlinear least-squares fits to a periodic waveform. The dashed lines are the best fit to the expected waveform shape produced by a triangular driving term in equation (5).

shows that any dependence of the island width on the beam orientation is weak. Out of a typical island width of 6–10 cm, the measured change in conditionally-averaged island width is only a few millimeters, $\lesssim 2\%$. Variability in the behavior for repeat shots is substantial (figures 11(*a*) and (*d*)).

To quantify the magnitude of the response more accurately, the data for each discharge are fit to a waveform with a 50 ms period. The uncertainties shown in figure 11 are used to create an ensemble of time-series data that are then fit by periodic waveforms. Table 1 shows the amplitude and phase of the fundamental component, including standard deviations derived from the ensemble. An amplitude of $\sim$1 mm is found for the cases with co-injection; the fundamental amplitude is nearly zero for the counter-current cases. Although the existence of a periodic component appears statistically significant for individual cases, shot-to-shot reproducibility is poor. A Bayesian uncertainty analysis of the two shots in figure 11(*a*) shows that the posteriors of the fits may be consistent but, for the three shots in figure 11(*d*), the means of the best fits are too widely separated to be consistent with one another. Unfortunately, checks on shot-to-shot reproducibility are only available for these two cases. We conclude that statistically significant variations in island width do not exceed $\lesssim$1 mm for any of the cases. The response of the island width to counter injection is especially small.

To assess the significance of these results, consider the generalized Rutherford equation for the island width $W$. It is of the form [41]

$$\frac{\tau_R}{r_s}\frac{\mathrm{d}W}{\mathrm{d}t} = r_s\Delta' + \beta_p r_s \frac{a}{W} + (\text{seed island term}) + (\text{fast-ion term}). \tag{2}$$

Here $\tau_R = \mu_0 r_s^2/1.22\eta_{\text{neo}}$ is the resistive diffusion time; $\eta_{\text{neo}}$ is the neoclassical resistivity. The first term on the right-hand side of the equation ($\Delta'$) represents the classical tearing mode parameter associated with the current profile. The second term is the destabilizing effect associated with helical perturbation of the bootstrap current at the $q = 2$ surface. The third term is important when the island width is small. The fourth term represents perturbed helical currents driven by fast ions [12–15]. We seek effects that could modulate $W$ at 20 Hz.

**Table 1.** Results of least-squares fitting to the data of figure 11. The second and third columns are the amplitude and phase of the fundamental component of arbitrary periodic waveforms. The fourth column is the amplitude of the solution of equation (5) when the RHS of the equation is a triangular waveform.

| Source | Amplitude (mm) | Phase (deg) | Model (mm) |
|---|---|---|---|
| On/Co/Tang | $1.4 \pm 0.4$ | $116 \pm 103$ | 0.6 |
| | $1.7 \pm 0.6$ | $126 \pm 101$ | 0.6 |
| Off/Co/Tang | $1.2 \pm 0.3$ | $14 \pm 7$ | 0.4 |
| On/Co/Perp | $1.0 \pm 0.3$ | $104 \pm 24$ | 0.9 |
| Off/Co/Perp | $1.2 \pm 0.5$ | $-109 \pm 41$ | −0.6 |
| | $0.9 \pm 0.4$ | $42 \pm 148$ | 0.9 |
| | $0.9 \pm 0.4$ | $-11 \pm 37$ | 0.0 |
| On/Ctr/Tang | $0.4 \pm 0.3$ | $87 \pm 74$ | 0.1 |
| On/Ctr/Perp | $0.4 \pm 0.4$ | $6 \pm 74$ | −0.3 |

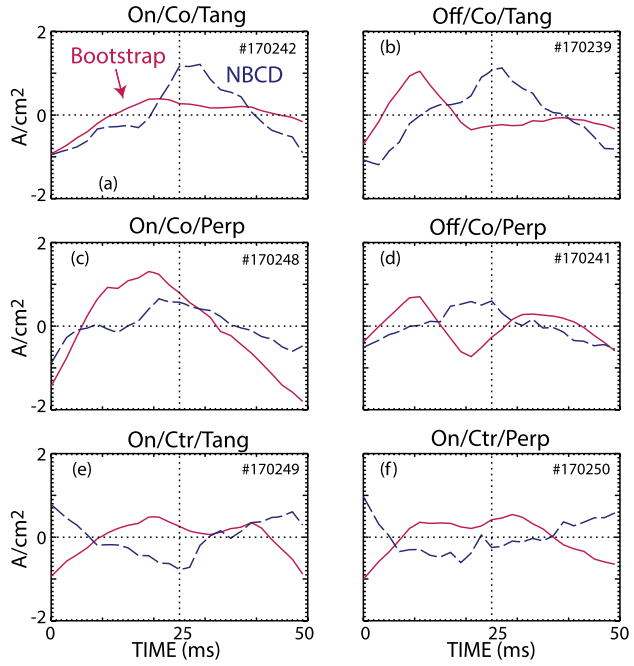


**Figure 12.** Classical conditionally-averaged bootstrap (solid) and beam-driven (dashed) currents at the $q = 2$ surface as calculated by TRANSP for the six different beam orientations. The format is the same as figure 11.

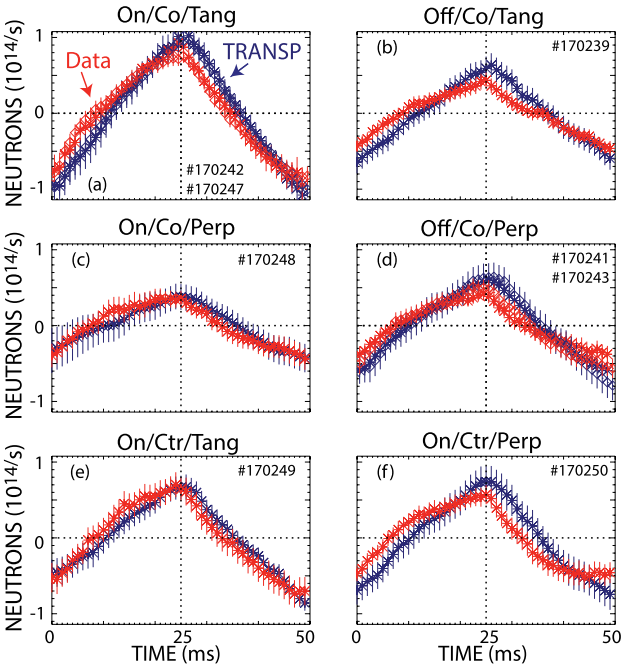


**Figure 13.** Conditionally averaged neutron rate and classical prediction for six different orientations of the neutral beams. The format is the same as figure 11.

Toroidal rotation is known to affect the island width [38]. The torque of the different neutral beam sources varies, so the toroidal rotation differs for the different sources. During a modulation cycle, the frequency changes $\pm 0.4$ kHz for on-axis injection with the co-tangential source. The change is of smaller magnitude for all of the other sources and of the opposite sign for the counter sources. Since the change is modest compared to the $\sim 10$ kHz average rotation and since, in any event, the effect of rotation on stability is relatively weak, changes in rotation are not expected to be a major effect.

The destabilizing helically perturbed bootstrap current is proportional to the pressure gradient at the $q = 2$ surface. The different modulated beams are likely to alter the pressure gradient $\mathrm{d}p/\mathrm{d}r$ differently; for example, an on-axis source might increase $|\mathrm{d}p/\mathrm{d}r|$, while an off-axis source might flatten the gradient. The TRANSP code calculates the axisymmetric bootstrap current. To assess the temporal modulation of the bootstrap current, kinetic profiles are fit every 5 ms through many modulation cycles for six representative discharges. The conditionally-averaged modulated bootstrap current calculated by TRANSP is shown in figure 12. The amplitude of the modulation is on the order of 10% of the $\sim 10$ A cm$^{-2}$ average bootstrap current at $q = 2$, so could cause a measurable change.

Currents driven by fast ions could impact stability. The TRANSP code also calculates the axisymmetric neutral-beam driven current. The average value of the neutral-beam driven current at $q = 2$ is $\sim 25$ A cm$^{-2}$ for these discharges. Since this current is larger than the bootstrap current, if the TMs cause modifications in beam-driven current, modulated changes in width might be apparent. Figure 12 shows the conditionally-averaged modulated beam current at the $q = 2$ surface.

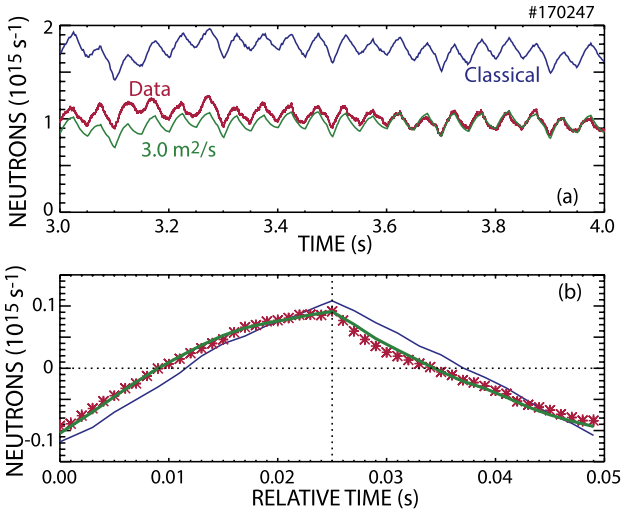


**Figure 14.** (*a*) TRANSP predictions of the neutron rate with and without anomalous beam-ion diffusion. A value of $D_B = 3.0$ m$^2$ s$^{-1}$ agrees well with the measurement. (*b*) Conditional average of the predictions and data over the 3.0–4.0 s time interval. The prediction with ad hoc diffusion accurately reproduces the measured waveform.

To infer an approximate upper bound on the importance of fast-ion effects, rewrite equation (2) as

$$\frac{\tau_R}{r_s}\frac{\mathrm{d}W}{\mathrm{d}t} = r_s\Delta' + \frac{(b+f)r_s}{W}, \qquad (3)$$

where we have dropped the seed-island term, represented the bootstrap term by $br_s/W$, and assumed that the fast-ion contribution $fr_s/W$ has the same functional dependence on island width as the bootstrap term, as suggested by the

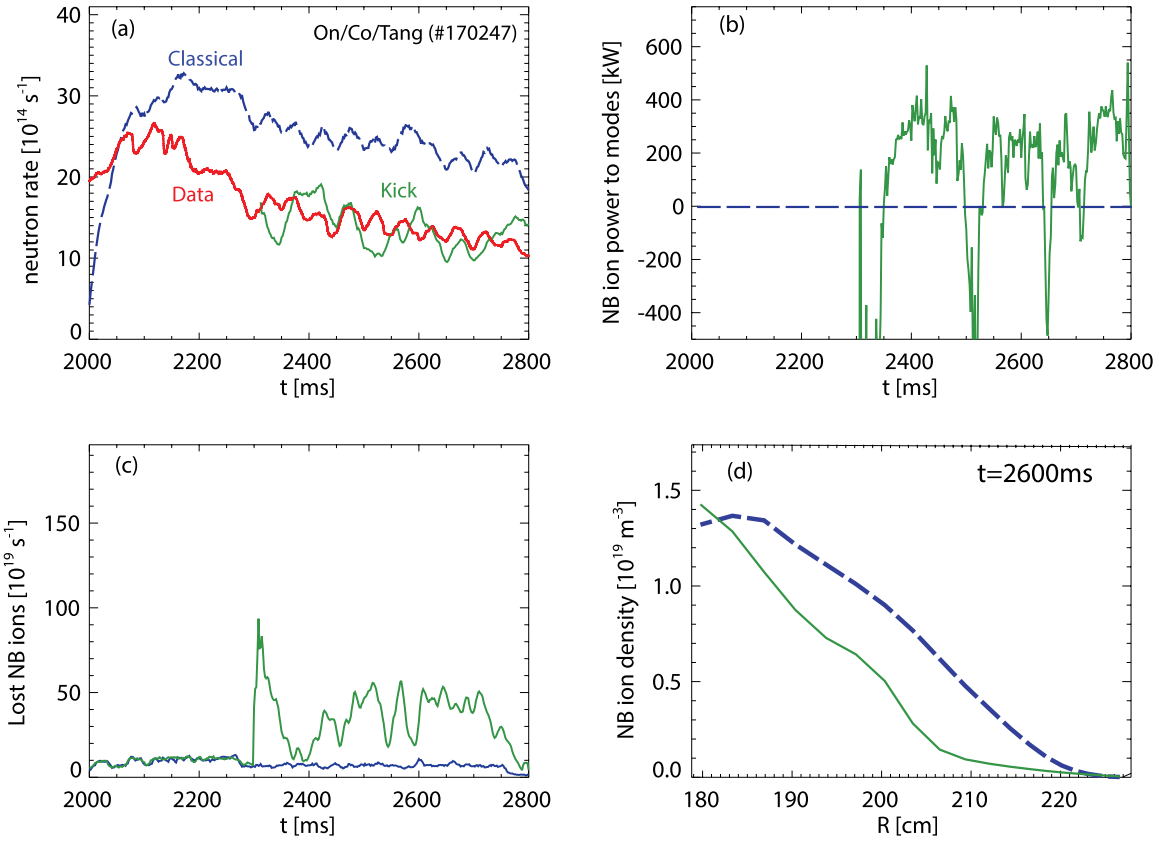


**Figure 15.** Results of the TRANSP kick modeling. (*a*) Neutron rate predicted by the TRANSP kick model when using experimentally measured mode widths; the data and the classical prediction are also shown. (The kick prediction begins near 2300 ms.) (*b*) Calculated power transferred from the fast ions to the modes. (*c*) Lost fast ions versus time. The flat line near zero are the losses in the classical case. (*d*) Classical (dashed) and kick (solid) fast-ion density profiles.

analysis of Hegna and Bhattacharjee [12]. Assume the effect of modulation is small, as suggested by the data, so each function can be written as the sum of a large steady-state contribution and a smaller modulated portion; e.g. $W = W_0 + W_1$, with $W_1 \ll W_0$. Since the current diffusion time is very long compared to 50 ms, direct modification of $\Delta'$ through change in the current profile is assumed negligible, so the first-order perturbation of the $\Delta'$ term is neglected. The steady-state (zeroth-order) equation implies that the saturated island width is $W_0 = (b_0 + f_0) r_s/(-\Delta' r_s)$. Neglecting higher-order terms, in first order, equation (3) becomes

$$\frac{\tau_R}{r_s}\frac{\mathrm{d}W_1}{\mathrm{d}t} + \frac{(b_0+f_0)r_s}{W_0^2}W_1 \simeq \frac{(b_1+f_1)r_s}{W_0}. \qquad (4)$$

This equation is of the form

$$\tau\frac{\mathrm{d}w}{\mathrm{d}t} + w = F(t), \qquad (5)$$

where $\tau \equiv \tau_R(W_0/r_s)^2/(b_0+f_0)$, $w = W_1/W_0$, and $F(t) \equiv (b_1+f_1)/(b_0+f_0)$. Equation (5) is a first-order inhomogeneous ordinary differential equation for the modulated island width $w$. Since the data are conditionally averaged over many cycles, transients associated with the complementary solution are unimportant; we desire the particular solution that is driven by modulation of the helical bootstrap ($b_1$) and fast-ion ($f_1$) currents.

To solve equation (5), we must specify the form of the periodic driving term $F(t)$. The waveform of the modulated beam is a square wave centered about its average power but the driven bootstrap and fast-ion currents are expected to have differently shaped waveforms. Ignore the perturbed bootstrap current term $b_1$, although a waveform could be fit to the data of figure 12. Presumably the fast-ion driven current $f_1$ depends on the details of the modulated distribution function but, for simplicity, assume that $f_1$ is proportional to the total number of fast ions: This implies that $f_1$ is a triangle waveform. Note that the triangular shape of the computed axisymmetric driven currents in figures 12(*a*) and (*b*) are consistent with this assumption.

Typical values for this experiment are $\tau_R \simeq 1000$ ms, $W_0/r_s \simeq 0.3$, and $b_0 \simeq 0.6$, so the characteristic time $\tau$ in equation (5) is greater than 100 ms. For a 50 ms modulation period, this implies that the second term on the LHS of equation (5) is small, so the predicted modulation $w$ is essentially the integral of the driving term $F(t)$. The best fit to the expected waveform for a triangle-shaped driving term is overlaid on the data in figure 11. The agreement with the predicted waveform is poor. The amplitude of the best fits are tabulated in the final column of table 1. Here, a positive (negative) amplitude indicates a stabilizing (destabilizing) contribution by the modulated source.

The poor agreement can be used to infer an upper bound on the magnitude of the perturbed fast-ion effect. Taking $|W_1| \leqslant 1$

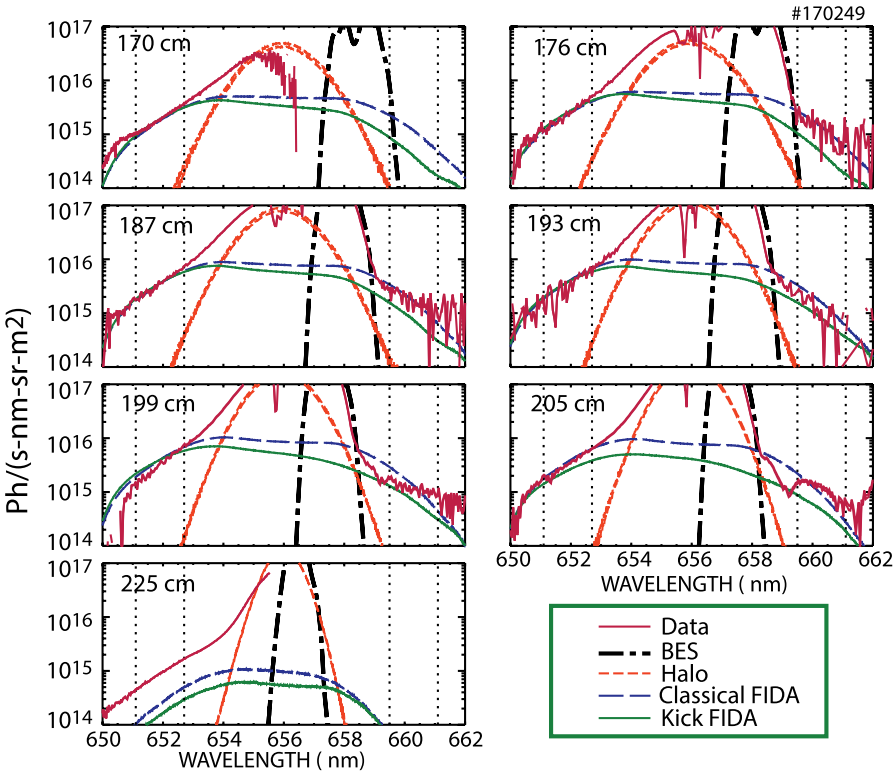


**Figure 16.** Predicted and measured FIDA spectra for seven spatial channels. The separate contributions to the spectra predicted by FIDASIM are shown: beam emission from the active beam (BES, dot–dash line), thermal emission (Halo, short-dash line), fast-ion emission predicted classically (Classical FIDA, long-dash line), fast-ion emission predicted using the 'kick' distribution function (Kick FIDA, solid line). The dotted vertical lines show the blue-shifted and red-shifted wavelength integration windows employed in figure 18. The data are the time-averaged (2.4–3.75 s) net signal (beam-on minus beam-off) with ELMs removed.

mm, the ratio of the perturbed fast-ion current to the steady-state bootstrap term $f_1/b_0$ is $\lesssim$0.2. This is not a particularly stringent limit. Owing to the rather large characteristic time $\tau$ for the island width to respond to changes in the driving terms, the width is insensitive to modulation with a period that is shorter than $\tau$. Future experiments should employ longer modulation periods.

It should be noted that existing theories of the effect of fast ions on mode stability [12–15] utilize a steady-state slowing-down distribution, not a modulated distribution function. Comparisons of modulated data with theory require a time-dependent treatment.

In summary, a definitive phase-space dependent effect on mode stability is *not* observed in this experiment.

## 4. Effect of TMs on fast-ion confinement

Conditionally-averaged neutron signals for the six different beam orientations are compared with classical TRANSP predictions in figure 13. Deviations between the experimental and theoretical waveforms indicate fast-ion transport from the phase-space volume measured by the neutrons [20]. In all cases, the data are more rounded than the triangular-shaped classical predictions. Statistically significant deviations occur for many beam orientations, suggesting that the tearing modes cause transport in much of phase space. For two beam orientations, multiple discharges are available; these cases are overlaid in figures 13(*a*) and (*d*) and give very similar results. Another check on the data is to use different averaging intervals; this also gives similar results.

The deviations in average neutron rate (figure 10) and in the modulated waveforms (figure 13) imply substantial fast-ion transport. The use of ad hoc fast-ion diffusion in TRANSP quantifies the magnitude of the transport empirically. A spatially and temporally constant value of $D_B = 3.0$ m$^2$ s$^{-1}$ provides a good fit to both the average neutron rate and to the conditionally averaged waveform (figure 14); this value is relatively large for DIII-D. (A 7% better fit to the average rate is obtained for $D_B = 2.5$ m$^2$ s$^{-1}$, while $D_B = 3.5$ m$^2$ s$^{-1}$ provides a slightly better fit to the conditionally averaged waveform.) The excellent fit in figure 14(*b*) suggests that the principal effect of the TMs is spatial diffusion. This is in contrast to the data collected during strong Alfvén eigenmode activity, which could *not* be described by ad hoc diffusion alone [20].

In contrast to ad hoc diffusion, the TRANSP kick model [42, 43] is a physics-based, reduced model for fast-ion transport by instabilities. Here, the TRANSP kick model is used in 'interpretive' mode, i.e. mode amplitudes are based on experimentally measured values. The mode structure is modeled by the analytical form of [7]. In addition to the primary (2,1) mode, three smaller amplitude modes are also included. Figure 2 shows the resulting kick probabilities for ions near the injection energy. The predicted energy kicks are strongest for trapped ions, counter-passing ions are next, and co-passing

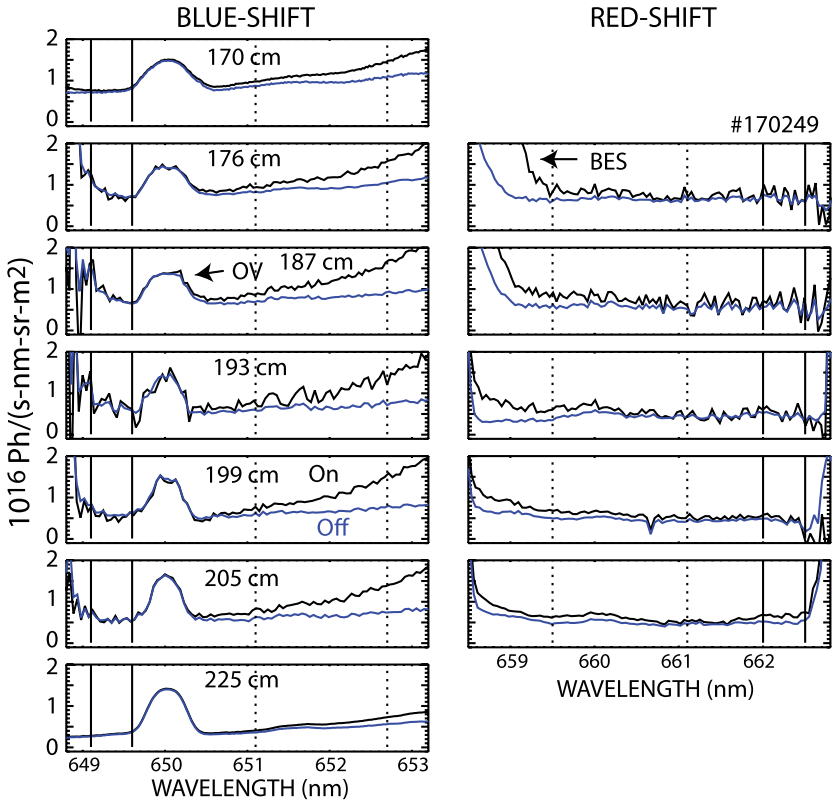


**Figure 17.** Blue-shifted (left column) and red-shifted (right column) FIDA data for seven spatial channels. The two curves in each panel are the time-averaged (2.4–3.75 s) spectra when the active beam is on (upper black trace) and when the active beam is off (lower blue trace). The dotted vertical lines show the wavelength integration windows used in figure 18. The solid vertical lines show the wavelength integration windows used to estimate the offset error. Spectra on the red-shifted side are only available for five spatial channels. The large signal near 659 nm for the innermost channels is from beam emission. An oxygen impurity line appears at 650.024 nm.

ions suffer the smallest kicks. For simplicity, any transport associated with Alfvén eigenmodes is ignored.

Figure 15 shows the result of the kick analysis using the experimentally measured mode amplitude from ECE. The kick model successfully reproduces the average neutron rate (figure 15(*a*)). The model predicts that fast ions deliver ∼200 kW to the TMs (figure 15(*b*)). (The average injected power is 12.1 MW in this discharge.) A substantial increase in fast-ion losses is also predicted (figure 15(*c*)). (Including charge-exchange losses, the calculated losses are over three times larger than the classical case and are a substantial fraction of the injected power.) The TM-induced transport causes significant narrowing of the fast-ion profile; the fast-ion density near $q = 2$ is approximately half of the classical value (figure 15(*d*)).

Analysis of FIDA data is challenging for these conditions. The frequent ELMs and strong instabilities cause large temporal variations in background light. On most shots, the active beam was on constantly while other beams were modulated but the temporal variations in background produce random error that overwhelms meaningful variations in FIDA signal. The only useful FIDA data are from the discharge where the active beam was modulated. For this case, analysis begins by eliminating timeslices with ELMs, then average 'beam-on' and 'beam-off' spectra are calculated. Net signals for the seven available channels are shown in figure 16, together with predictions from the synthetic diagnostic code FIDASIM [44].

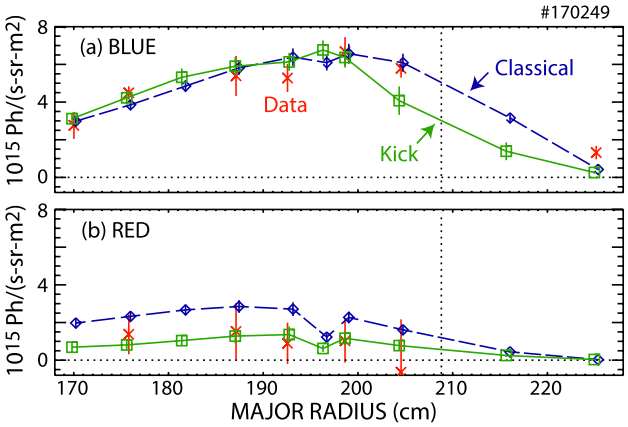


**Figure 18.** (*a*) Blue-shifted and (*b*) red-shifted FIDA spatial profiles from measurements (x), classical predictions (diamond, dashed-line) and kick-model predictions (square, solid line). For the theory, the error bars are the standard deviation of the mean over the averaging interval (2.4–3.75 s). The dashed vertical location is the approximate location of the $q = 2$ surface. For the data, the error bars combine the standard deviation of the mean over the averaging interval with the estimated offset error, added in quadrature. The blue-shifted data are integrated between wavelengths of 651.1–652.7 nm and the red-shifted data between 659.5–661.1 nm.

The distribution function computed by TRANSP NUBEAM is input to FIDASIM for the calculation of the FIDA component of the spectrum. For most channels, the predicted FIDA light is similar on the blue-shifted side of the spectrum (below

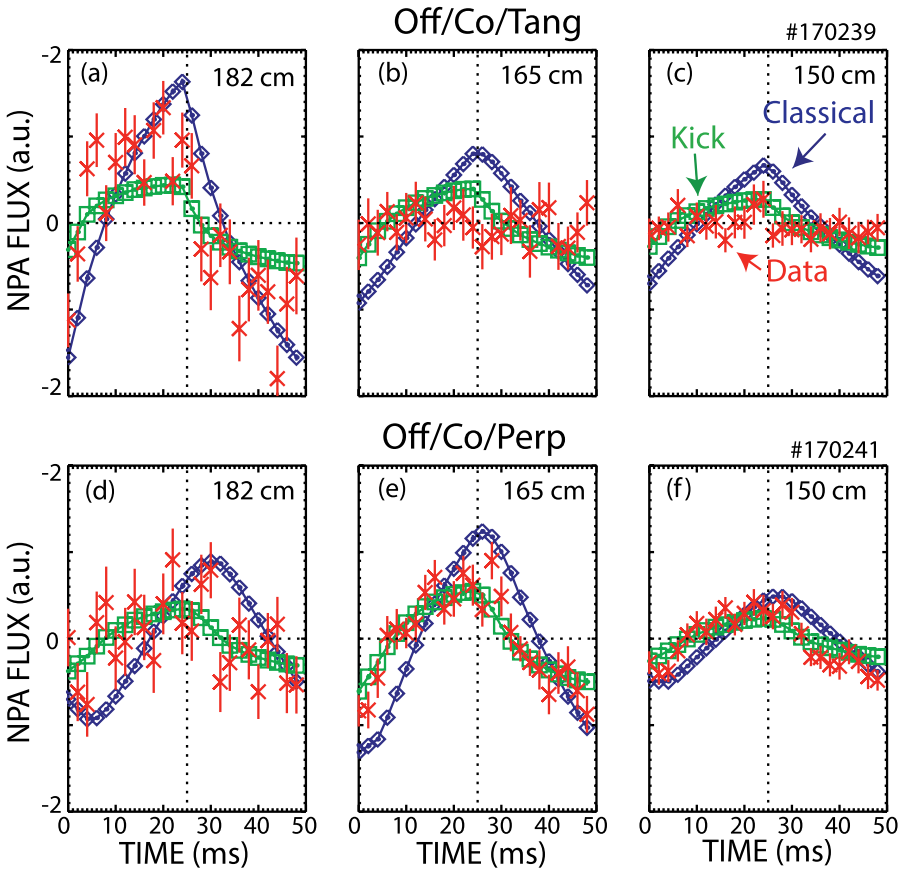


**Figure 19.** Conditionally-averaged NPA signals (x) for modulated off-axis tangential (top row) and perpendicular (bottom row) sources. The classical (diamond) and kick-model (square) predictions are also shown. The NPA channels are labeled by their midplane crossing: $(a, d)$ $R = 182$ cm, $(b, e)$ $R = 165$ cm, and $(c, f)$ $R = 150$ cm.

656.1 nm) for both the classical and the kick distribution functions but, on the red-shifted side of the spectrum (above 656.1 nm), the kick model predicts a substantial reduction in signal. Recalling the weight functions (figure 3), this difference reflects the strong transport of counter-passing ions in the kick model.

Figure 17 show the spectra in greater detail. On the blue-shifted side of the spectrum, with increasing wavelength, the beam-on signal rises above the beam-off signal, a clear signature of a FIDA feature. The maximum injection energy is 81 keV, so no FIDA signal is predicted below ~650.0 nm and, as expected, the net signal (beam-on minus beam-off) is very small at large blue-shifted Doppler shifts. In contrast, on the red-shifted side of the spectrum, apart from the beam-emission feature, the beam-on and beam-off signals are rather similar, so the net FIDA signal is small. The difference between beam-on and beam-off signals at large Doppler shifts provides an estimate of offset errors in background subtraction.

Figure 18 displays radial profiles on the blue-shifted and red-shifted sides of the spectrum after integration over wavelength. The absolute calibration of the signal is from an in-vessel calibration during an earlier vacuum vent. An *in situ* check on the intensity calibration using an MHD-quiescent discharge was performed two months prior to the TM experiment and gives excellent agreement with the classical FIDASIM prediction for all but the outermost ($R = 225$ cm) chord. (Because of this discrepancy, this channel is excluded from further consideration.) On the blue-shifted side that is most sensitive to co-passing ions, the data agree well with both the classical and the kick predictions on most of the channels but, on the red-shifted side, the agreement is much better with the kick model (reduced $\chi^2 = 0.91$ for the classical prediction and $\chi^2 = 0.55$ for the kick model). The data indicate that transport of counter-passing ions by the TMs is strong.

**Table 2.** Available data for this experiment. Each diagnostic measures both an average ('steady-state') signal and a conditionally-averaged ('modulated') signal. Where meaningful comparisons with the TRANSP kick model are possible, the figure number is listed. For the neutrons, the modulated signal was used to infer the time evolution of the TM amplitude. For the conditionally-averaged FIDA data, the signal-to-noise ratio is poor. The average NPA data cannot be directly compared to the theoretical prediction because of uncertainty in the absolute calibration.

| Diagnostic | Data | Result |
|---|---|---|
| Neutrons | Average | Figure 15(*a*) |
| | Modulated | Used for TM amplitude |
| FIDA | Average | Figure 18 |
| | Modulated | Poor signal-to-noise |
| NPA | Average | No absolute calibration |
| | Modulated | figure 19 |

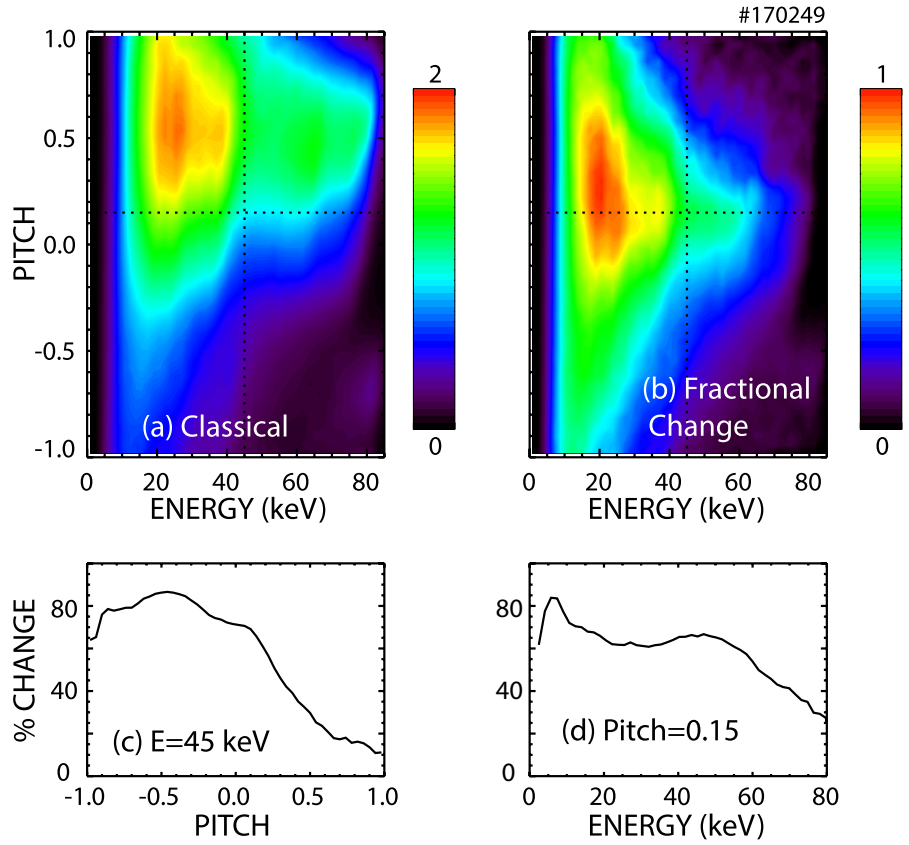


**Figure 20.** (*a*) Velocity-space dependence of the classical distribution function $f_c$ after summing over spatial coordinates. (*b*) Difference between the classical and kick distribution functions $f_c - f_k$. The maximum of the color map is half as large in panel (*b*) as in panel (*a*). The dotted lines show the 'cuts' through the distribution plotted in the lower row. (*c*) Percentage difference $100(f_c - f_k)/f_c$ of the classical and kick distribution functions at 45 keV versus pitch. (*d*) Percentage difference $100(f_c - f_k)/f_c$ at a pitch of 0.15 versus energy. In TRANSP, positive pitch $v_{\|}/v$ is in the direction of the plasma current.

Analysis of the NPA data is also challenging. For a typical case, the passive contribution to the signal is 1.4 times larger than the active contribution. The data are processed to remove high-frequency noise and to interpolate over ELMs. Useful data are available for two discharges with very long stationary periods of 1.4 and 1.7 s, respectively. To achieve excellent phase-space resolution in the theoretical calculations, the TRANSP distribution functions are calculated with $10^6$ Monte Carlo markers for the modulated source and are saved every 2.5 ms; after processing by FIDASIM, the theoretical predictions are conditionally averaged over the same time intervals as the data. The active beam is on steadily during the entire time interval. Since the NPA diagnostic is not absolutely calibrated, the signals are multiplied by normalization factors obtained from similar shots that had modulated active beams. (The selected normalization factors are conservative: the actual modulated signals may be even smaller than shown in figure 19.)

The results of this analysis appear in figure 19. The modulated signals are smaller than predicted classically, indicating loss of trapped fast ions from the portion of phase space interrogated by the diagnostic. The data agree far better with the kick model than with the classical prediction. Quantitatively, the reduced $\chi^2$ of the 150 measurements in figure 19 is 1.4 for the kick model and 4.4 for the classical prediction. The data are inconsistent with the classical prediction but in reasonable agreement with the kick model.

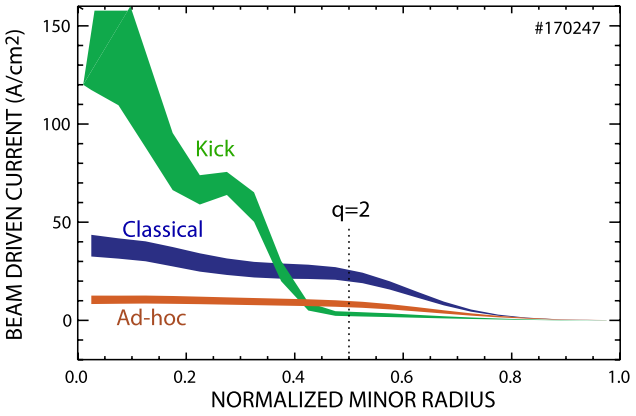


**Figure 21.** TRANSP calculations of neutral-beam current density versus normalized minor radius for the classical, kick model, and ad hoc diffusion of 3.0 $m^2$ $s^{-1}$ (dash-dot line) distribution functions. The shaded areas span one standard deviation in the time interval between 2.4–2.75 s. The dotted vertical line indicates the location of the $q = 2$ surface.

Table 2 summarizes the data that are available for comparison with the TRANSP kick model. Despite (a) the presence of AEs, (b) TRANSP uncertainties associated with uncertainties

in plasma parameters, (c) approximations in the treatment of the TMs and (d) the approximations inherent in the kick model, all available data are consistent with the predictions.

In light of the success of the TRANSP kick model in reproducing the neutron, FIDA, and NPA data, it is of interest to examine the calculated changes in the distribution function. Figure 20(*a*) shows the classically-expected distribution function in velocity space after integration over configuration space. The classical distribution function extends up to the injection energy (81 keV) and consists predominately of co-passing ions. Figure 20(*b*) shows the difference between the classical and kick distribution functions. The distribution is strongly modified, with changes of $\sim$50% in much of phase space. The changes are larger for trapped and counter-passing particles (pitch $\lesssim$0.3) than for co-passing particles (figure 20(*c*)). As expected for a diffusive, cumulative process, the changes are larger for lower energies than energies near the injection energy (figure 20(*d*)).

## 5. Discussion and conclusion

Qualitatively, the effect of the fast ions on mode stability is modest (section 3) but the effect of the modes on fast-ion confinement is large (section 4). This contrasts sharply with the results of a recent study of the interaction of fast ions with Alfvén eigenmodes (AE) using similar techniques. In that work, modulation of a single source caused $O(10\%)$ changes in AE amplitude during the modulation cycle [20, 22]. Large transport was observed when overlapping wave-particle resonances caused the orbits to become stochastic but the transport was small when only a few modes were unstable [21, 23]. The situation is different for TMs. In the plasma frame, the modes are essentially stationary. Some fast-ion orbits resonate with the TMs but the density of resonances in phase space is sparse. On the other hand, the amplitude of the field perturbation is much larger than for the AEs. The TM spoils the tokamak axisymmetry, in a manner similar to toroidal field ripple or a poorly designed stellarator, so spatial diffusion is greatly enhanced.

The effect of the TMs is more complicated than pure spatial diffusion, however. Figure 21 compares the calculated profiles of beam-driven current when using the classical distribution function, the distribution function found by the kick model, and the distribution function from spatial diffusion alone. Because the kick model preferentially affects trapped and counter-passing ions, it predicts a threefold enhancement in on-axis co-driven current density. (The total change in beam-driven current is much smaller, about 8%.) In contrast, large spatial diffusion suppresses neutral-beam current drive. Clearly, a proper treatment of velocity space is crucial for accurate calculations of beam-driven current [45]. Although this qualitative conclusion is surely correct, it should be noted that the results shown in figure 21 are not entirely self-consistent. All of the calculations use the experimental kinetic and $q$ profiles measured in the presence of the TM. If the TM was absent, the profiles would change, altering the classical prediction.

The amplitude of the (2,1) TM in this experiment is large, more than 10% of the minor radius. These plasmas with poor fast-ion confinement are *not* an attractive operating scenario for magnetic fusion! Attractive 'hybrid' operating scenarios have TMs of higher mode number and smaller amplitude [1, 2] and, presumably, much smaller fast-ion transport. The large (2,1) TM employed in this experiment was selected to give measurable effects on the fast-ion diagnostics.

The effort to perform 'whole device modeling' of tokamak plasmas should include modeling of TMs. The results presented here suggest that a fairly accurate model can be readily implemented in TRANSP. The relatively weak effect of fast ions on mode stability suggests that a standard generalized Rutherford equation can be employed to predict the mode width. The good agreement of the TRANSP kick model with the fast-ion measurements using an analytical form for the mode structure suggests that, using the mode width predicted by the Rutherford equation, the kick model can provide an accurate description of the TM-induced transport. Work to test the TRANSP kick model under a wider set of plasma conditions and to develop a predictive capability is underway.

## Acknowledgments

We thank the entire DIII-D team for their support and Eric Fredrickson for helpful suggestions. This material is based upon work supported by the U.S. Department of Energy, Office of Science, Office of Fusion Energy Sciences, using the DIII-D National Fusion Facility, a DOE Office of Science user facility, under Award DE-FC02-04ER54698. DIII-D data shown in this paper can be obtained in digital format by following the links at https://fusion.gat.com/global/D3D_DMP.

## Appendix. Orbit-based weight functions

The purpose of a weight function is to identify the phase-space sensitivity of a particular diagnostic measurement. The paper that first introduced the concept made the ansatz that the signal $S$ is the integral over velocity space of the weight function $W$ and the fast-ion distribution function $F$ [46],

$$S = \int W(\vec{v})F(\vec{v})\,\mathrm{d}\vec{v}. \tag{A.1}$$

A recent paper [27] placed this ansatz on a rigorous footing and generalized it to encompass the spatial dependence of the distribution function. The chosen phase-space coordinates in that work are the energy $E$, the maximum major radius of the orbit $R_m$, and the pitch $p_m = v_\parallel/v$ of the fast ion at $R_m$. In this formalism, the weight function is related to the probability that a particular orbit $(E, R_m, p_m)$ produces a signal at the detector.

Of course, real detectors are sensitive to multiple orbits. Also, as in figure 3, it may be desirable to represent the weight function in other phase-space coordinates, such as $(E, \mu, P_\phi)$. Each orbit makes a contribution $S_i$ to the measured signal. The weight functions $W$ plotted in figure 3 are the $S_i$-weighted kernel density estimates $\hat{f}$ of all of the orbits near a particular

location in $(\mu, P_\phi)$ phase space, normalized by the Jacobian $\mathcal{J}$ associated with the coordinate transformation between $(E, R_m, p_m)$ coordinates and $(E, \mu, P_\phi)$ coordinates,

$$W(\mu, P_\phi) = \hat{f}(\mu, P_\phi)/\mathcal{J}(\mu, P_\phi), \tag{A.2}$$

where

$$\hat{f}(\mu, P_\phi) = \frac{1}{N}\sum_i^N S_i k_h(\mu - \mu_i, P_\phi - P_{\phi,i}), \tag{A.3}$$

$k_h$ is a scaled kernel function (a gaussian in this case), $N$ is the number of calculated orbits, and $(\mu_i, P_{\phi,i})$ are the coordinates of the $i$-th orbit. The Jacobian is found by calculating the kernel density estimate for uniform diagnostic weights, $S_i = 1$.

In practice, all four signals represented in figure 3 include an explicit or implicit integral over energy so, in calculating the kernel density estimate, it is necessary to impose a limit on the energies that contribute to the signal. In figure 3, an energy limit of the maximum injection energy is employed. Note that, since multiple orbits with different energies contribute to the measured signals, it is not possible to include accurate topological boundaries in figure 3.

## ORCID iDs

M. Podestà https://orcid.org/0000-0003-4975-0585

## References

[1] Wade M.R. *et al* 2005 *Nucl. Fusion* **45** 407
[2] Staebler A. *et al* 2005 *Nucl. Fusion* **45** 617
[3] Heidbrink W.W. and Sadler G.J. 1994 *Nucl. Fusion* **34** 535
[4] Carolipio E.M., Heidbrink W.W., Forest C.B. and White R.B. 2002 *Nucl. Fusion* **42** 853
[5] Zweben S.J. *et al* 1999 *Nucl. Fusion* **39** 1097
[6] García-Munoz M. *et al* 2007 *Nucl. Fusion* **47** L10
[7] Gobbin M. *et al* 2009 *Nucl. Fusion* **49** 095021
[8] Konovalov S.V. and Putvinskii S.V. 1988 *Sov. J. Plasma Phys.* **14** 461
[9] Mynick H.E. 1993 *Phys. Fluids* B **5** 2460
[10] Forest C.B. *et al* 1997 *Phys. Rev. Lett.* **79** 427
[11] Marchenko V.S. and Lutsenko V.V. 2001 *Phys. Plasmas* **8** 4834
[12] Hegna C.C. and Bhattacharjee A. 1989 *Phys. Rev. Lett.* **63** 2056
[13] Cai H. *et al* 2011 *Phys. Rev. Lett.* **106** 075002
[14] Cai H. and Fu G. 2012 *Phys. Plasmas* **19** 072506
[15] Cai H. 2016 *Nucl. Fusion* **56** 126016
[16] Sesnic S. *et al* 2000 *Phys. Plasmas* **7** 935
[17] Fredrickson E.D. 2002 *Phys. Plasmas* **9** 548
[18] Li E. *et al* 2016 *Plasma Phys. Control. Fusion* **58** 045012
[19] Anderson J.K. *et al* 2013 *Phys. Plasmas* **20** 056102
[20] Heidbrink W.W. *et al* 2016 *Nucl. Fusion* **56** 112011
[21] Collins C.S. *et al* 2016 *Phys. Rev. Lett.* **116** 095001
[22] Heidbrink W.W. *et al* 2017 *Phys. Plasmas* **24** 056109
[23] Collins C.S. *et al* 2017 *Nucl. Fusion* **57** 086005
[24] Murakami M. *et al* 2009 *Nucl. Fusion* **49** 065031
[25] Muscatello C.M., Heidbrink W.W., Taussig D. and Burrell K.H. 2010 *Rev. Sci. Instrum.* **81** 10D316
[26] Zhu Y.B., Bortolon A., Heidbrink W.W., Celle S.L. and Roquemore A.L. 2012 *Rev. Sci. Instrum.* **83** 10D304
[27] Stagner L. and Heidbrink W.W. 2017 *Phys. Plasmas* **24** 092505
[28] Carlstrom T.N., Ahlgren D.R. and Crosbie J. 1988 *Rev. Sci. Instrum.* **59** 1063
[29] Zeng L. *et al* 2006 *Nucl. Fusion* **46** S677
[30] Carlstrom T.N. *et al* 1992 *Rev. Sci. Instrum.* **63** 4901
[31] Austin M.E. and Lohr J. 2003 *Rev. Sci. Instrum.* **74** 1457
[32] Gohil P., Burrell K.H., Groebner R.J. and Seraydarian R.P. 1990 *Rev. Sci. Instrum.* **61** 2949
[33] Lao L.L., St. John H., Stambaugh R.D., Kellman A.G. and Pfeiffer W. 1985 *Nucl. Fusion* **25** 1611
[34] Rice B.W., Nilson D.G. and Wroblewski D. 1995 *Rev. Sci. Instrum.* **66** 373
[35] King J.D. *et al* 2014 *Rev. Sci. Instrum.* **85** 083503
[36] Tobias B. *et al* 2010 *Rev. Sci. Instrum.* **81** 10D928
[37] Bardóczi L. *et al* 2016 *Phys. Plasmas* **23** 052507
[38] Lahaye R.J. and Sauter O. 1998 *Nucl. Fusion* **38** 987
[39] Pankin A., Mccune D., Andre R., Bateman G. and Kritz A. 2004 *Comput. Phys. Commun.* **159** 157
[40] Heidbrink W.W. *et al* 2014 *Plasma Phys. Control. Fusion* **56** 095030
[41] Sauter O. *et al* 1997 *Phys. Plasmas* **4** 1654
[42] Podesta M., Gorelenkova M. and White R.B. 2014 *Plasma Phys. Control. Fusion* **56** 055003
[43] Podestà M. *et al* 2017 *Plasma Phys. Control. Fusion* **59** 095008
[44] Heidbrink W.W., Liu D., Luo Y., Ruskov E. and Geiger B. 2011 *Commun. Comput. Phys.* **10** 716
[45] Podestà M. *et al* 2015 *Nucl. Fusion* **55** 053018
[46] Heidbrink W.W. *et al* 2007 *Plasma Phys. Control. Fusion* **49** 1457